PHOTONICS Research

Stimulated generation of deterministic platicon frequency microcombs

Hao Liu,[1,5,†] Shu-Wei Huang,[1,2,†] Wenting Wang,[1] Jinghui Yang,[1] Mingbin Yu,[3] Dim-Lee Kwong,[3] Pierre Colman,[4] and Chee Wei Wong[1,6]

[1]Fang Lu Mesoscopic Optics and Quantum Electronics Laboratory, University of California Los Angeles, Los Angeles, California 90095, USA
[2]Department of Electrical, Computer, and Energy Engineering, University of Colorado Boulder, Boulder, Colorado 80309, USA
[3]Institute of Microelectronics, Singapore, Singapore
[4]Université de Bourgogne Franche-Comté, ICB, UMR CNRS 6303, Dijon, France
[5]e-mail: haoliu1991@ucla.edu
[6]e-mail: cheewei.wong@ucla.edu

Received 28 March 2022; revised 13 May 2022; accepted 15 May 2022; posted 16 May 2022 (Doc. ID 459403); published 22 July 2022

Dissipative Kerr soliton generation in chip-scale nonlinear resonators has recently observed remarkable advances, spanning from massively parallel communications, to self-referenced oscillators, and to dual-comb spectroscopy. Often working in the anomalous dispersion regime, unique driving protocols and dispersion in these nonlinear resonators have been examined to achieve the soliton and soliton-like temporal pulse shapes and coherent frequency comb generation. The normal dispersion regime provides a complementary approach to bridge the nonlinear dynamical studies, including the possibility of square pulse formation with flattop plateaus, or platicons. Here we report observations of square pulse formation in chip-scale frequency combs through stimulated pumping at one free spectral range and in silicon nitride rings with +55 fs^2/mm normal group velocity dispersion. Tuning of the platicon frequency comb via a varied sideband modulation frequency is examined in both spectral and temporal measurements. Determined by second-harmonic autocorrelation and cross correlation, we observe bright square platicon pulse of 17 ps pulse width on a 19 GHz flat frequency comb. With auxiliary-laser-assisted thermal stabilization, we surpass the thermal bistable dragging and extend the mode-locking access to narrower 2 ps platicon pulse states, supported by nonlinear dynamical modeling and boundary limit discussions.

https://doi.org/10.1364/PRJ.459403

1. INTRODUCTION

Over the past two decades, remarkable breakthroughs have been seen in the chip-scale frequency microcomb [1–5] studies with ultrahigh-Q microresonators [6–12], from tabletop demonstrations [13,14] to small factor integrated platforms [15–17], thriving in both fundamental dynamics [14,18–26] and various applications including spectroscopy [27], optical coherent tomography (OCT) [28,29], low noise radio frequency generation [30,31], frequency synthesis [15], distance ranging [32,33], and high-speed optical communication [34–36]. Most of these works are based on dissipative Kerr solitons (DKS) in anomalous group velocity dispersion (GVD) microresonators for self-referenced broadband optical frequency combs, which requires a delicate balance between loss and gain, as well as nonlinear phase and dispersion [37], and could limit the pulse energy if an ultrashort pulse and a broadband spectrum are desired simultaneously. Since the material GVDs of most platforms are normal in visible and near-infrared frequency ranges, the cavities are often engineered to achieve anomalous dispersion in pump resonances across a broad range [21,38,39]. Among these platforms, silicon nitride stands out due to its CMOS-compatible fabrication process, large Kerr nonlinearity, broad transparent window, low Raman nonlinearity, and high-power handling capability [37]. The engineering of silicon nitride is commonly based on a thick-nitride (>600 nm) waveguide that supports multiple transverse modes to achieve anomalous dispersion while maintaining high quality factors for low threshold frequency microcomb generation [17,40]. However, the inevitable coupling between different transverse mode families characteristically modulates the amplitude of the frequency microcomb spectrum and could detrimentally destabilize the dissipative Kerr soliton formation [9,41]. A tapered waveguide is then proposed to achieve anomalous GVD and single-mode operation simultaneously [42,43]; however, the operation for DKS remains nontrivial [17,44,45] with complex intracavity dynamics [22,23,46]. Furthermore, the ultralow-loss thick-nitride waveguide fabrication needs special treatment [47], which is not offered in current commercial Si_3N_4 foundry

process. Consequently, the adoption of DKS in standard photonic integrated circuit (PIC) architectures through commercial foundries is still not possible [48]. Compared to the state-of-the-art ultralow-loss thick-nitride Si_3N_4 microresonator with 30 million Q [49], recent demonstrations of ultrathin silicon nitride microresonators have achieved 260 million Q with comparable free spectral range (FSR) [50], which significantly decreases the microcomb generation threshold. However, anomalous dispersion is forbidden in such schemes. Consequently, the study of novel methods to enhance normal dispersion frequency microcomb generation can simplify the microresonator frequency comb architecture and extend its operation into other frequency ranges.

Frequency microcomb generation in the normal GVD regime has recently been examined both theoretically and experimentally in a variety of platforms including crystalline resonators and integrated microresonators [21,51–54], and it has also been demonstrated in many applications [35,55,56]. Its formation and nonlinear dynamics usually require shifted pump mode resonances [57], which can be achieved by avoiding the mode crossing caused by mode coupling between different mode families [58] or coupling between adjacent microresonators [59,60], or self-injection locking [48,56] to provide local anomalous dispersion [9,54]. Among these prior studies, a solitonic bright pulse with unique flattop square pulse shape—or the platicon—has increasingly drawn attention in numerical studies [57,61,62]. These theoretical modeling studies on the platicon have shown its pulse width can be continuously controlled in a broad range via the pump-resonance detuning (and hence the intracavity energy and nonlinear parametric gain). In addition, the conversion efficiency of pump power into comb power can be potentially higher in the platicon comb than in solitons for the same GVD value [57]. Benefitting from its optical spectra's sharp edge and flattop features, the platicon can help increase the signal processing capabilities in optical domain for high-speed communication [63–65] with other applications in pulse shaping and amplification, nonlinear optical imaging, and production of high-brightness electron beams [66]. Although experimental demonstration of platicon frequency microcombs via self-injection locking has been recently demonstrated via self-injection locking [48] and pulse-pumping [67], the platicon generation via intensity-modulated pump [68], to the best of our knowledge, has not yet been demonstrated.

Here we experimentally demonstrate the generation of a platicon frequency microcomb and its operating parameters in a chip-scale Si_3N_4 microresonator with normal dispersion as a follow-up to our previous demonstration [69]. Via an intensity-modulated pump [68], a platicon generation approach is demonstrated such that sophisticated schemes for introducing pump mode shift or self-injection locking could be avoided. A platicon frequency comb with an 80 nm span (60 dB intensity roll-off) and clean comb spacing beat note is achieved. The pump-to-comb conversion efficiency is around 21%. The platicon has a flattop pulse duration deterministically tunable from 2 to 17 ps, observed and confirmed through optical spectra, intensity autocorrelation, and dual-comb cross-correlation measurements. Controls of the frequency comb optical spectrum through third-order dispersion (TOD), pump-resonance detuning, and modulation frequency are studied and characterized.

2. THEORETICAL STUDY OF THE PLATICON DYNAMICS VIA MODULATED PUMP

To understand and predict the nonlinear dynamics, we first start with a modified form of the Lugiato–Lefever equation (LLE), which has an intensity-modulated external pump to numerically model the platicon generation:

$$T_R\frac{\partial}{\partial t}A(t,\tau)=\sqrt{\alpha_c}A_P-\left[\frac{\alpha_c+\alpha_p}{2}+j\delta-jL_{\text{cav}}\times\sum_{k\geq 2}\frac{\beta_k}{k!}\left(j\frac{\partial}{\partial\tau}\right)^k-j\gamma I(t,\tau)\right]A(t,\tau),\quad(1)$$

where T_R is the round-trip time, $A(t,\tau)$ is the envelope function of the platicon, t is the slow time corresponding to the evolution time over round trips, τ is the fast time describing the temporal structure of the wave, A_P is the external pump, α_p is the propagation loss, α_c is the coupling loss, δ is the pump-resonance detuning, and ω_c and ω_p are the cavity resonance frequency and pump frequency, respectively. β_k describes the dispersion coefficient ($\beta_2>0$ indicates normal GVD, and $\beta_2<0$ indicates anomalous GVD), and we only consider second- and third-order dispersion in this case for simplicity. $\gamma=\frac{n_2\omega_0}{cA_{\text{eff}}}$ is the Kerr nonlinearity, in which n_2 is the nonlinear refractive index and A_{eff} is the effective modal area of the pumping transverse mode. In our modified LLE, we assign $A_P=\sqrt{P\{1+M\sin[\frac{2\pi t}{T_R}(\frac{\Delta}{\omega_{\text{FSR}}}+1)]\}}$ to describe the intensity-modulated external pump, where P is the pump power without modulation, M is the modulation depth ($0\leq M\leq 1$), and $\Delta=\omega_M-\omega_{\text{FSR}}$ is the deviation between the modulation frequency ω_M and the FSR $\omega_{\text{FSR}}=\frac{2\pi}{T_R}$ of the pumped cavity resonance. The simulation starts from vacuum noise and is run for 1.5×10^5 round trips until the solution reaches a steady state. The parameters used in the simulation are from the cold cavity characterization, where the FSR is 19.548 GHz with normal GVD of +55 fs^2/mm and negative TOD of −948 fs^3/mm.

The formation of platicon with an intensity-modulated pump can be explained by wave-breaking theory [70–72] as detailed below. Figure 1(a) shows the 2D evolution map of platicon temporal profile against the non-dimensional cavity resonance detuning δ, with four snapshots of the 2D illustrated in Fig. 1(b). Figure 1(b_1) ($\delta=-0.1$) shows the sinusoidal envelope of the modulated pump input seeding the wave-breaking dynamics. Resulting from self-phase modulation, the pump ahead and behind the modulation minimum respectively experiences an instantaneous frequency upshift and downshift. In a normal GVD microresonator, such difference in the frequency shift leads to deceleration and acceleration of the pump ahead and behind the modulation minimum. Consequently, evolution of the initially sinusoidal envelope would be directed outward around modulation maxima and inward around the modulation minima, leading to self-steepening around the modulation minima [72], such as shown in Fig. 1(b_2) ($\delta=+0.0334$). The wave is thus compressed, and four-wave mixing (FWM) of the front of the pulse further

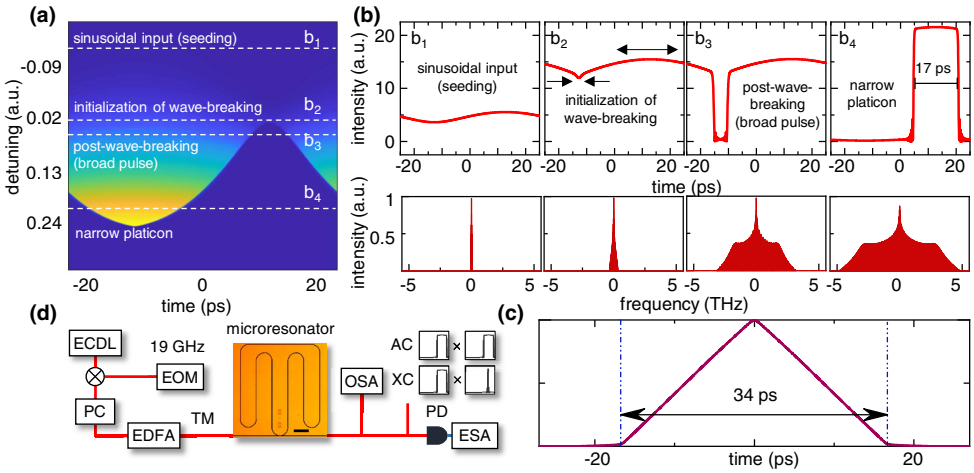

Fig. 1. Platicon pulse generation in normal-dispersion frequency combs: operating regimes, numerical modeling, and modulated pump experimental setup. (a) 2D evolution map of platicon temporal profile as a function of intracavity fast time and detuning. Four characteristic stages are selected to show the details of the evolution in panel (b). (b) Upper panels: temporal profiles of the platicon at different evolution stages; lower panels: frequency spectra corresponding to each state. (b_1) Sinusoidal input (seeding); (b_2) initialization of wave breaking. Self-steepening shows that wave breaking is about to happen, with modulation maxima directed outwardly and minima directed inwardly. (b_3) Post-wave breaking. Wave breaking happens, and a broad square pulse is generated; (b_4) a shorter narrow platicon is generated for increasing red detuning, such as at $\delta = +0.2531$. (c) The simulated autocorrelation of the square pulse shown in (b_4). The width of the triangle is twice of the width of the square pulse. (d) Schematic setup of platicon generation. The cw laser from the ECDL is first modulated by an EOM, and the modulation frequency is chosen to match the single FSR (≈19.547 GHz). After amplification by an EDFA, the modulated pump is launched into the single-mode microresonator, and the pump frequency is slowly red-tuned to generate the platicon. A polarization controller (PC) and a polarized beam splitter (not shown in the diagram) are utilized to optimize the intensity of TM polarization for TM mode operation. A 20 GHz high-speed photodetector (PD) is used to measure the amplitude and phase noises. An OSA is used to map the platicon spectrum. Then the time-domain dynamics is examined by both autocorrelation (AC) and dual-comb cross correlation (XC). The actual single-mode microresonator is shown in the middle micrograph, whose straight waveguide is tapered from 2.5 to 1 μm to maintain high quality factor. The curved regions are 1 μm in width to maintain our single-mode frequency comb operation. Scale bar: 200 μm.

broadens the comb spectrum, wherein the wave-breaking initialization occurs. This subsequently results in a bright and wide square pulse generation (pulse maxima spanning over a longer time scale) as shown in Fig. 1(b_3) ($\delta = +0.0598$). With further red detuning ($\delta = +0.2531$), the bright square pulse duration decreases down to 17 ps as shown in Fig. 1(b4). Thus, after the occurrence of the wave breaking, the platicon pulse width shortens with increasing pump-cavity resonance red detuning, while the peak intensity of the pulse increases as well.

The corresponding simulated frequency microcomb spectra are shown in the lower row of each intermediate state. We note that, in the platicon state, the comb lines have a somewhat flat plateau away from the pump wavelength with roughly uniform intensities, before gradually decreasing to the noise floor. In our numerical modeling plots, the y-axis range is chosen such that it is comparable to the experimental dynamic range in our optical spectrum analyzer (OSA). We put a 17 ps simulated platicon for better illustration of the square shape characteristics; however, the pulse width is theoretically controllable from tens of picoseconds (ps) to sub-ps level, by simply varying the detuning. Since the 17 ps pulse has a square temporal structure, its computed autocorrelation is triangular as shown in Fig. 1(c), with the bottom width of the triangle twice the platicon square pulse width. The triangular structure in the autocorrelation helps distinguish if a platicon is generated in the time domain.

3. EXPERIMENTAL INVESTIGATION OF PLATICON VIA MODULATED PUMP

For our experiments, we utilize a single-mode Si_3N_4 microresonator nanofabricated in a CMOS-compatible foundry, with FSR of 19 GHz, Q factor of 1.2 million, and symmetrically top-bottom cladded with SiO_2. Through high-resolution coherent swept wavelength interferometry [51], the GVD is measured to be normal at 55 ± 2.5 fs^2/mm. Figure 1(d) subsequently shows the schematic setup for our measurements: the pump from a tunable external cavity diode laser (ECDL) is sent into an electro-optical modulator (EOM) with 20 GHz bandwidth. The modulation frequency, provided by a local oscillator (LO), is set at 19.548 GHz to closely match the cold cavity FSR of the microresonator at pump wavelength, and the modulation depth is set so that the sideband intensity is about 3 dB lower than the pump intensity. After amplification by an erbium-doped fiber amplifier (EDFA), the polarization of the modulated pump is carefully controlled by a fiber polarization controller (PC), and a polarized beam splitter maximizes the intensity of the pump projected into the TM mode. Then the modulated pump with an on-chip power up to 1.4 W is launched into the microresonator. The output is collected by optical and electronic spectrum analyzers to measure the optical spectra, amplitude noises, and radio frequency beat notes, respectively. Intensity autocorrelation and dual-comb cross-correlation measurements are conducted to

analyze the time-domain performance of the platicon frequency comb.

A. Platicon Generation via Modulated Pump

We first experimentally study the evolution of the platicon frequency microcomb, with modulation frequency set at 19.548 GHz, close to the 19 GHz single FSR. We red-tune the pump frequency in steps of 5 MHz to generate the platicon. The GVD and TOD measurements of the selected microresonator are shown in Fig. 2(a) right inset. Figure 2(a) shows the triangular pump power transmission versus different pump-resonance detuning. States 1 (red) and 4 (black) are before and after the platicon generation, with their reference optical spectra (solely from the modulated pump) shown in the left inset of Fig. 2(a). The center pump is about 3 dB higher in power than in the first sideband pair. As the pump laser is frequency-tuned into the cavity resonance, the platicon frequency comb starts to evolve. At the beginning, the cascaded FWM of the modulated pump leads to a weak growth of higher-order sidebands with characteristic rapid power decay for increasing mode numbers away from the pump. This is illustrated in the green curve of Fig. 2(b). With further tuning into the cavity resonance, the comb spectrum is dramatically broadened as shown in the blue curve of Fig. 2(b). The platicon spectrum shows the signature characteristic plateau and is supported by our wave-breaking modeling shown earlier in Fig. 1(b). To illustrate the difference between the platicon spectrum and the soliton spectrum, we plot a simulated single soliton spectrum with similar pump power, which is the orange dashed line in Fig. 2(b). It indicates that the platicon could not only achieve higher comb line power at wavelengths away from the pump but also has a flatter comb spectrum. The widest platicon comb spectrum generated by a single modulated pump is observed at the critical point of state 3, spanning over 80 nm (60 dB intensity roll-off) and matches our numerically modeled estimate of 82 nm [left inset of Fig. 2(b)]. The calculated pump to comb conversion efficiency is about 21%. Subsequently, with further increase of the pump wavelength, the platicon comb is lost, and the spectrum drops back to the modulated pump line as shown earlier in state 4.

B. Effect of Modulation Frequency-FSR Deviation Δ

To elucidate the underlying physics of the platicon formation, we next examined the impact of Δ on the platicon frequency comb spectrum. This is shown in Figs. 3(a)–3(c) (modeling) and Figs. 3(d)–3(f) (measurements). The platicon is robust under a range of Δ values, which effectively controls the spectral symmetry and intensity distribution of the comb lines. We consider the modeled platicon spectral characteristics prior to the measurements and for the three cases of zero TOD, negative TOD, and positive TOD. Here we use skewness from statistics for reference to describe the symmetry of platicon comb spectra. We assign the comb line wavelength λ_i as the variable, where the pump wavelength λ_{pump} is the mean, and the value $P_i = \frac{I_i}{I_{\text{total}}}$ of the log-scale comb line intensity normalized to the total intensity is the probability for each comb line. Then the skewness is defined as skewness $= \frac{\mu_3 - 3\mu\sigma^2 - \mu^3}{\sigma^3}$, where $\mu_3 = \sum_i \lambda_i^3 P_i$, $\mu = \sum_i \lambda_i P_i$, and $\sigma^2 = \sum_i \lambda_i^2 P_i - \mu^2$. In our cases, zero skewness indicates a perfectly symmetric comb spectrum, while negative skewness indicates that more comb line power distributes on the longer wavelength (lower frequency), and positive skewness means more comb line power distributes on the shorter wavelength (higher frequency). In the first and conceptual case of zero TOD, our modified LLE

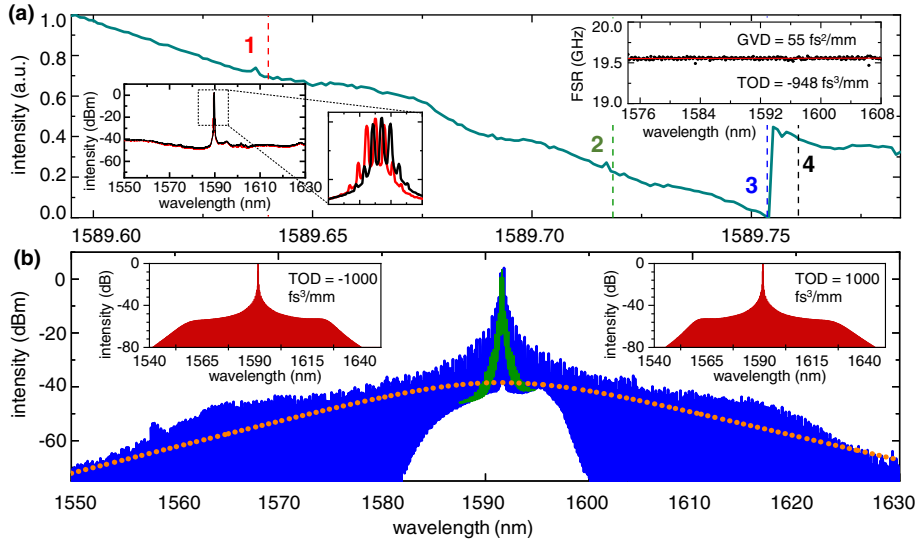

Fig. 2. Dynamic detuning evolution and spectra of a modulated-pump platicon frequency comb. (a) Pump transmission versus detuning. The comb evolves to its critical point at state 3 (blue). Left inset: optical spectra of states 1 (red) and 4 (black), in which there are only modulated pump spectra. The first pair of sidebands are about 3 dB in intensity lower than main pump. Right inset: FSR measurement of the microresonator. The fitted GVD is positive at 55 fs^2/mm, and the fitted TOD is negative at −948 fs^3/mm. (b) Comb spectra at states 2 and 3. The comb just starts to evolve due to spontaneous FWM at state 2 (green curve), and the spectrum shape is more like a triangle other than the frequency spectrum of a platicon. At state 3, the frequency comb spectrum (blue curve) is at the critical point, spanning 80 nm. The shape coincides with the simulation, shown in the upper left inset. The upper right inset is comb spectrum simulation with positive TOD as a comparison. A typical single-soliton comb spectrum envelope is included in the dashed pink line, indicating that the platicon has higher comb line power at wavelengths away from the pump.

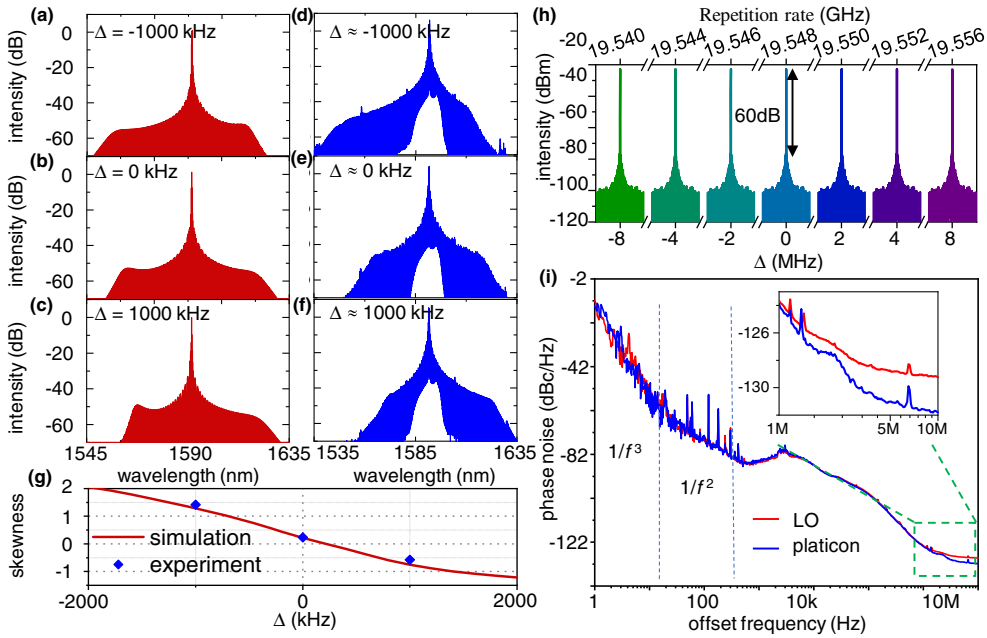

Fig. 3. Deterministic platicon comb formation controlled by the sideband modulation frequency. (a)–(c) Simulated frequency comb spectra with different modulation frequencies under a TOD of −1000 fs^3/mm. (a) $\Delta = -1000$ kHz, (b) $\Delta = 0$ kHz, (c) $\Delta = 1000$ kHz. (d)–(f) Experimental frequency comb spectra with different modulation frequencies. (d) 19.547 GHz ($\Delta \approx -1000$ kHz), (e) 19.548 GHz ($\Delta \approx 0$ kHz), (f) 19.549 GHz ($\Delta \approx 1000$ kHz). All comb spectra span around 80 nm. (g) Comb skewness versus sideband modulation frequency Δ. (h) Heterodyne beat note of the platicon frequency microcomb at different modulation frequency. The x axis is the offset frequency with respect to the FSR of pump mode. A 60 dB SNR is observed for each case. The RBW is 1 kHz. (i) Phase noise measurements of the LO and platicon comb. The phase noise of the platicon comb almost exactly follows the phase noise of the LO in the low-frequency range; except in the $1/f^3$ range, the platicon is slightly better. But starting from 1 MHz, the platicon comb outperforms the LO and suppresses the phase noise by up to 3 dB.

modeling shows that Δ will affect the comb line distribution; hence the symmetry of the comb spectra. Since the comb spectrum is perfectly symmetric at $\Delta = 0$, the impact of Δ on the comb line distribution is symmetrical around the zero point. We then examine the case of negative TOD at −1000 fs^3/mm, matching our microresonator measurements [−948 fs^3/mm shown in top right inset of Fig. 2(a)] and dispersion modeling, which is around −1000 fs^3/mm. When Δ is negative, the spanning of the comb spectrum on the left-hand side is significantly extended; hence, more comb lines are generated on the shorter wavelength side since the modulation frequency better matches the higher-frequency FSR (shorter wavelength) due to positive GVD. This is shown in Fig. 3(a) for the case of $\Delta = -1000$ kHz. The comb span on the shorter wavelength side is almost 45 nm wider than on the longer wavelength side, resulting in the platicon spectral asymmetry and more toward the blue side.

Figure 3(b) shows that, when $\Delta = 0$ kHz, the platicon microcomb is restored to a more symmetric spectrum, spanning 80 nm. The skewness in Fig. 3(g) indicates that, due to the presence of the TOD, the comb spectrum is not perfectly symmetric. However, there will be certain number of Δ that could compensate for the effect of the TOD, leading to skewness of zero. In Fig. 3(c), when $\Delta = 1000$ kHz, we see that the comb shape is asymmetric in an opposite manner (red weighted) and has a distinctly narrower comb compared to the former two cases. This is due to the Δ and negative TOD both contributing to decreasing the phase-matching bandwidth of the FWM. We note that, in each of the three Δ cases [Figs. 3(a)–3(c)], the general feature of the temporal square pulse is still captured in our simulations. In the case of zero and positive TOD, along with different Δ, the phenomenon is inverted, and the platicon spectral asymmetry is at the opposite frequencies.

In the experiment, due to thermal effect at high pump power, the FSR of the cavity will no longer be the same as the cold cavity characterization. For simplicity, here we still use 19.548 GHz for the Δ calculation. Figures 3(d)–3(f) show our platicon measurements for three different modulation frequencies with Δ of −1000, 0, and 1000 kHz. The general structure of the comb matches the numerical predictions remarkably. In Fig. 3(d) ($\Delta \approx -1000$ kHz), we observe the blue-weighted platicon comb spectrum; in Fig. 3(e) the symmetric comb spectrum is observed. In Fig. 3(f) ($\Delta \approx 1000$ kHz), the red-weighted platicon is achieved. We note that with a 2 MHz change in the modulation frequency, the platicon comb span is tuned by 20 nm and has a controllable blue-red weightage distribution of the platicon frequency comb. We also note that the modulation frequency should not deviate too much from the single FSR; otherwise, the broadband platicon comb is no longer observable.

C. Time-Domain Performance Characterization

Next we examine the stability of the platicon comb and its time-domain characteristic of the platicon at stage 3. It is worth mentioning that since the comb spacing is intrinsically locked

to the modulation frequency and there are no subcomb families, the amplitude noise remains intrinsically low, and the electrical beat note remains clean with high signal-to-noise ratio (SNR) throughout the whole evolution. Figure 3(h) shows the measured power spectral density of the comb spacing beat note with a resolution bandwidth (RBW) of 1 kHz, centered at the ≈19.548 GHz modulation frequency. No other frequency components are observed. Differing from traditional dissipative Kerr solitons, the platicon is naturally mode-locked, avoiding modulation instability and high-noise chaotic comb states. Figure 3(i) subsequently shows the platicon phase noise compared to the LO reference: at lower offset frequencies such as below 1 MHz, the platicon comb phase noise follows the LO almost exactly, with the platicon slightly worse than the LO in the flicker frequency ($1/f^3$) region below 180 Hz. However, starting from ≈1 MHz in our case, the platicon comb surpasses the phase noise character of the reference LO by up to 3 dB. Since this offset frequency is much lower than the cavity resonance linewidth (≈157 MHz), this phase noise suppression should not be from the filtering effect of the resonator but rather a phase noise low-pass filtering effect of the frequency comb, similar to Ref. [73].

The 60 dB SNR of the platicon beat note suggests that the frequency comb is phase-locked and potentially mode-locked. To verify the mode-locking, we next examine the intensity autocorrelation (AC) of the platicon in a colinear scheme,

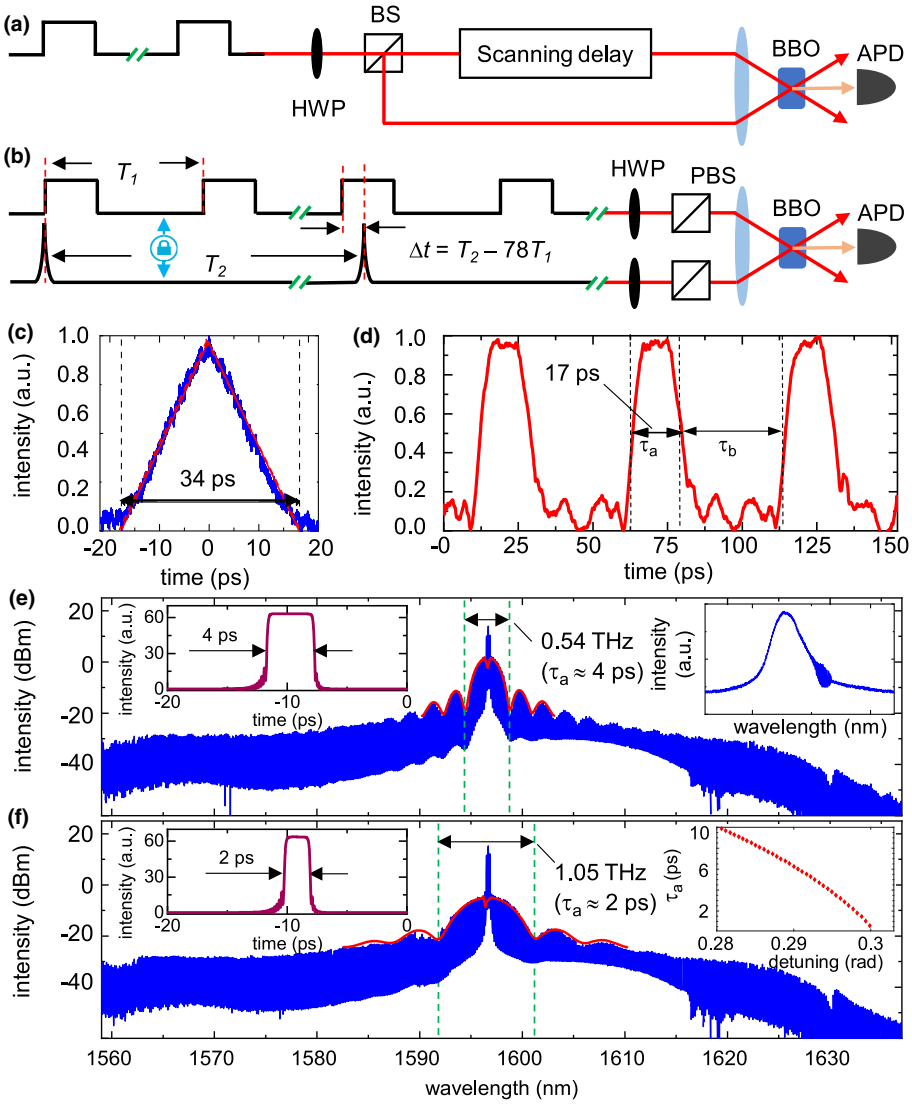

Fig. 4. Pulse width characterization of platicon square pulses. (a) Schematic autocorrelation setup. BS, beam splitter; HWP, half-wave plate; APD, avalanche photodetector. (b) Schematic cross-correlation setup. PBS, polarized beam splitter. (c) Time-domain autocorrelation of the platicon comb. The bottom width of 34 ps of the triangle shape indicates a square bright pulse of 17 ps. (d) Cross correlation of the platicon pulse frequency comb. A 17 ps square bright pulse is directly observed. (e) Comb spectrum of a 4 ps platicon square pulse. The spacing between the two first minima is about 0.54 THz. The experimental measurement matches well with the simulation platicon comb spectrum (red curve). The inset is the time-domain square pulse simulation corresponding to the red curve, which proves a 4 ps square pulse generation. (f) Comb spectrum of a 2 ps platicon square pulse. The simulation of both the frequency and time domains shows a 2 ps square pulse generation. Left inset is the time-domain profile. Right inset is a summary of the platicon pulse widths versus δ, which indicates that narrow pulse width down to hundreds of femtoseconds could be achieved.

depicted in Fig. 4(a). The platicon is split into two paths and then recombined on a bulk barium borate (BBO) for second-harmonic generation (SHG). The SHG signal is then collected by a 700 Hz femtowatt avalanche photodiode (APD). For a square pulse, the time-domain autocorrelation is triangular in structure. The measured autocorrelation in Fig. 4(c) shows a triangular shape with bottom width of 34 ps, indicating that a bright square pulse of 17 ps. Since this is a wide pulse, we implemented a dual-comb cross correlation (XC) to depict the pulse shape. Figure 4(b) depicts the schematic setup of the XC measurement. Different from the AC setup, we utilize a 250 MHz fiber laser frequency comb (Menlo) as the sampling pulse. The pump modulation frequency (and thus the platicon frequency comb spacing) and the Menlo fiber reference laser comb spacing are both referenced to the same Rb-disciplined crystal oscillator. By tuning the Menlo fiber laser comb spacing close to 1/78 of the modulation frequency, dual-comb XC can be achieved due to the temporal walk-off between the picosecond platicon (period T_1) and the femtosecond reference pulse (period T_2). The two locked pulse trains will have a time lag $\Delta t = T_2 - 78T_1$ after every 78 cycles of the square pulse train. With both stable pulses trains sent into two half-wave plates (HWPs) and polarization beam splitters (PBS) and then aligned into the BBO for SHG, the cross-correlation sampled signal is collected by the APD. A high-speed oscilloscope is then used to record the platicon temporal shape. The platicon pulse is depicted in Fig. 4(d). Sampled over 100 pulses, the dual-comb cross-correlated pulse width τ_a is gauged to be around 17 ps, and the repetition period $(\tau_a + \tau_b)$ is observed to be 51 ps.

D. Extended Access to Platicon States via a Dual-Driven Scheme

As previously mentioned, the pulse width of the platicon square pulse can be controlled by varying the pump-resonance detuning. The nonlinear thermal effect of the microresonator, however, introduces thermal bistable dragging when sweeping the pump across the resonance; this hinders us from accessing the effective red-detuning side of the resonance, where narrower square pulses can exist. Hence, we implemented an auxiliary-laser-assisted thermal stabilization method [45] to overcome the thermal bistability. By sending an auxiliary pump backward into a resonance in the C-band at the blue-detuned regime and fixing the wavelength of the auxiliary pump, the microresonator is heated. Then a single-FSR intensity modulated pump is tuned into a resonance in the L-band in a forward direction. With more power launched into the resonance, the resonance further redshifts, pushing the aux pump out of the resonance, effectively cooling the microresonator, and vice versa. Such balance effectively achieves thermal stabilization of the resonance, with appropriate auxiliary pump power (at least 2 dB higher than the main pump in our case), making access to the red-detuned regime accessible. Narrower deterministically tuned pulse widths are successfully achieved. Figures 4(c) and 4(d) show the frequency comb spectra with pulse widths of ≈4 ps and ≈2 ps, respectively. The inset of Fig. 4(e) shows the pump transmission with auxiliary pump. The strong modulation of the comb spectrum arises from the Fourier nature of square pulse, which manifests itself as a sinc function in the frequency domain. The size of the main dome (first-minima spacing and bounded by the two vertical dashed blue lines as shown) uniquely corresponds to the pulse width τ_a. Figure 4(e) shows a 0.54 THz spacing, which corresponds to a 4 ps square platicon. The frequency-domain simulation (red envelope) matches the measurement almost exactly, which bridges the comb spectrum measurement to the corresponding time-domain simulation (inset figure). Figure 4(f) shows another achieved dual-pumped comb state with a 1.05 THz dome size, a Fourier shape that corresponds to the generation of a 2 ps square platicon. As previously discussed, the platicon pulse τ_a could be continuously changed by changing the detuning between the pump frequency and the resonance frequency. The inset of Fig. 4(d) shows the simulation of the pulse width versus the detuning below 10 ps. The narrowest pulse width achievable with current simulation parameters is ≈616 fs. The inset shows that the pulse width becomes more sensitive to the detuning as the pulse width gets narrower.

4. CONCLUSION

In this work we demonstrate the platicon frequency comb generation in normal GVD microresonators with a single-FSR intensity-modulated pumping scheme. Initiated from the wave-breaking dynamics, we analyze the influence of modulation frequency and pump-resonance detuning on the platicon frequency comb properties. A phase-locked and mode-locked frequency comb is observed, and the bright square pulse with widths from 2 to 17 ps is depicted using dual-comb XC. For the 17 ps platicon, the pump-to-comb conversion efficiency is about 21%. We demonstrate the comb symmetry deterministic control with the sideband modulation frequency, together with the TOD, along with the beat note power spectral density and phase noise character. With auxiliary-laser-assisted thermal stabilization, we extend access of "the forbidden regions" of platicon generation, observing narrow square pulse generation. The stabilized platicon comb also simplifies estimation of the platicon pulse width via stable by bridging the platicon comb spectrum features to its pulse width. The nonlinear microresonator is a unique platform for the study of wave breaking. This work has noteworthy influence on generating frequency microcombs in the normal dispersion regime and with applications such as an intensity-flattened spectral comb for high-rate optical communications, nonlinear optical imaging with fiber endoscopes, pulse shaping and amplification, dual-comb and Raman spectroscopy, and novel on-chip microwave synthesizers.

Funding. National Science Foundation (1741707, 1810506, 1824568); Office of Naval Research (N00014-16-1-2094); Air Force Office of Scientific Research (FA9550-15-1-0081).

Acknowledgment. The authors are grateful for the helpful discussions with Yongnan Li, James F. McMillan, Jinkang Lim, Abhinav Kumar Vinod, and Qingsong Bai. We also thank Prof. Andrew Weiner for comments on initial discussions of this work.

Author Contributions. H.L. and S.W.H. designed the experiments and analyzed the data. H.L. and S.W.H.

performed the experiments. S.W.H. and J.Y. designed the resonator, and M.Y. and D.L.K. fabricated the microresonator. W.W. helped on the phase noise measurement. H.L. and C.W.W. prepared the paper. All authors contributed to discussion and revision of the paper.

Disclosures. The authors declare no conflicts of interest.

Data Availability. Data underlying the results presented in this paper are not publicly available at this time but may be obtained from the authors upon reasonable request.

†These authors contributed equally to this paper.

REFERENCES

1. T. J. Kippenberg, R. Holzwarth, and S. A. Diddams, "Microresonator-based optical frequency combs," Science **332**, 555–559 (2011).
2. S. A. Diddams, K. Vahala, and T. Udem, "Optical frequency combs: coherently uniting the electromagnetic spectrum," Science **369**, eaay3676 (2020).
3. A. L. Gaeta, M. Lipson, and T. J. Kippenberg, "Photonic-chip-based frequency combs," Nat. Photonics **13**, 158–169 (2019).
4. C. Xiang, J. Liu, J. Guo, L. Chang, R. N. Wang, W. Weng, J. Peters, W. Xie, Z. Zhang, J. Riemensberger, J. Selvidge, T. J. Kippenberg, and J. E. Bowers, "Laser soliton microcombs heterogeneously integrated on silicon," Science **373**, 99–103 (2021).
5. L. Chang, S. Liu, and J. E. Bowers, "Integrated optical frequency comb technologies," Nat. Photonics **16**, 95–108 (2022).
6. B. J. M. Hausmann, I. Bulu, V. Venkataraman, P. Deotare, and M. Lončar, "Diamond nonlinear photonics," Nat. Photonics **8**, 369–374 (2014).
7. H. Jung, C. Xiong, K. Y. Fong, X. Zhang, and H. X. Tang, "Optical frequency comb generation from aluminum nitride microring resonator," Opt. Lett. **38**, 2810–2813 (2013).
8. P. Del'Haye, A. Schliesser, O. Arcizet, T. Wilken, R. Holzwarth, and T. J. Kippenberg, "Optical frequency comb generation from a monolithic microresonator," Nature **450**, 1214–1217 (2007).
9. T. Herr, V. Brasch, J. D. Jost, I. Mirgorodskiy, G. Lihachev, M. L. Gorodetsky, and T. J. Kippenberg, "Mode spectrum and temporal soliton formation in optical microresonators," Phys. Rev. Lett. **113**, 123901 (2014).
10. M. Pu, L. Ottaviano, E. Semenova, and K. Yvind, "Efficient frequency comb generation in AlGaAs-on-insulator," Optica **3**, 823–826 (2016).
11. Y. He, Q.-F. Yang, J. Ling, R. Luo, H. Liang, M. Li, B. Shen, H. Wang, K. Vahala, and Q. Lin, "Self-starting bi-chromatic $LiNbO_3$ soliton microcomb," Optica **6**, 1138–1148 (2019).
12. V. Brasch, M. Geiselmann, T. Herr, G. Lihachev, M. H. P. Pfeiffer, M. L. Gorodetsky, and T. J. Kippenberg, "Photonic chip-based optical frequency comb using soliton Cherenkov radiation," Science **351**, 357–360 (2016).
13. S.-W. Huang, J. Yang, J. Lim, H. Zhou, M. Yu, D.-L. Kwong, and C. W. Wong, "A low-phase-noise 18 GHz Kerr frequency microcomb phase-locked over 65 THz," Sci. Rep. **5**, 13355 (2015).
14. T. Herr, K. Hartinger, J. Riemensberger, C. Y. Wang, E. Gavartin, R. Holzwarth, M. L. Gorodetsky, and T. J. Kippenberg, "Universal formation dynamics and noise of Kerr-frequency combs in microresonators," Nat. Photonics **6**, 480–487 (2012).
15. D. T. Spencer, T. Drake, T. C. Briles, J. Stone, L. C. Sinclair, C. Fredrick, Q. Li, D. Westly, B. R. Ilic, A. Bluestone, N. Volet, T. Komljenovic, L. Chang, S. H. Lee, D. Y. Oh, M.-G. Suh, K. Y. Yang, M. H. P. Pfeiffer, T. J. Kippenberg, E. Norberg, L. Theogarajan, K. Vahala, N. R. Newbury, K. Srinivasan, J. E. Bowers, S. A. Diddams, and S. B. Papp, "An optical-frequency synthesizer using integrated photonics," Nature **557**, 81–85 (2018).
16. B. Shen, L. Chang, J. Liu, H. Wang, Q.-F. Yang, C. Xiang, R. N. Wang, J. He, T. Liu, W. Xie, J. Guo, D. Kinghorn, L. Wu, Q.-X. Ji, T. J. Kippenberg, K. Vahala, and J. E. Bowers, "Integrated turnkey soliton microcombs," Nature **582**, 365–369 (2020).
17. B. Stern, X. Ji, Y. Okawachi, A. L. Gaeta, and M. Lipson, "Battery-operated integrated frequency comb generator," Nature **562**, 401–405 (2018).
18. S.-W. Huang, J. Yang, S.-H. Yang, M. Yu, D.-L. Kwong, T. Zelevinsky, M. Jarrahi, and C. W. Wong, "Globally stable microresonator turing pattern formation for coherent high-power THz radiation on-chip," Phys. Rev. X **7**, 041002 (2017).
19. B. Yao, S.-W. Huang, Y. Liu, A. K. Vinod, C. Choi, M. Hoff, Y. Li, M. Yu, Z. Feng, D.-L. Kwong, Y. Huang, Y. Rao, X. Duan, and C. W. Wong, "Gate-tunable frequency combs in graphene–nitride microresonators," Nature **558**, 410–414 (2018).
20. Q.-F. Yang, X. Yi, K. Y. Yang, and K. Vahala, "Counter-propagating solitons in microresonators," Nat. Photonics **11**, 560–564 (2017).
21. X. Xue, Y. Xuan, Y. Liu, P.-H. Wang, S. Chen, J. Wang, D. E. Leaird, M. Qi, and A. M. Weiner, "Mode-locked dark pulse Kerr combs in normal-dispersion microresonators," Nat. Photonics **9**, 594–600 (2015).
22. M. Yu, J. K. Jang, Y. Okawachi, A. G. Griffith, K. Luke, S. A. Miller, X. Ji, M. Lipson, and A. L. Gaeta, "Breather soliton dynamics in microresonators," Nat. Commun. **8**, 14569 (2017).
23. X. Yi, Q.-F. Yang, X. Zhang, K. Y. Yang, X. Li, and K. Vahala, "Single-mode dispersive waves and soliton microcomb dynamics," Nat. Commun. **8**, 14869 (2017).
24. M. Karpov, M. H. P. Pfeiffer, H. Guo, W. Weng, J. Liu, and T. J. Kippenberg, "Dynamics of soliton crystals in optical microresonators," Nat. Phys. **15**, 1071–1077 (2019).
25. T. E. Drake, J. R. Stone, T. C. Briles, and S. B. Papp, "Thermal decoherence and laser cooling of Kerr microresonator solitons," Nat. Photonics **14**, 480–485 (2020).
26. A. K. Vinod, S.-W. Huang, J. Yang, M. Yu, D.-L. Kwong, and C. W. Wong, "Frequency microcomb stabilization via dual-microwave control," Commun. Phys. **4**, 81 (2021).
27. M.-G. Suh, Q.-F. Yang, K. Y. Yang, X. Yi, and K. J. Vahala, "Microresonator soliton dual-comb spectroscopy," Science **354**, 600–603 (2016).
28. X. Ji, X. Yao, A. Klenner, Y. Gan, A. L. Gaeta, C. P. Hendon, and M. Lipson, "Chip-based frequency comb sources for optical coherence tomography," Opt. Express **27**, 19896–19905 (2019).
29. P. J. Marchand, J. C. Skehan, J. Riemensberger, J. Ho, M. H. P. Pfeiffer, J. Liu, C. Hauger, T. Lasser, and T. J. Kippenberg, "Soliton microcomb based spectral domain optical coherence tomography," Nat. Commun. **12**, 427 (2019).
30. S.-W. Huang, J. Yang, M. Yu, B. H. McGuyer, D.-L. Kwong, T. Zelevinsky, and C. W. Wong, "A broadband chip-scale optical frequency synthesizer at 2.7×10^{-16} relative uncertainty," Sci. Adv. **2**, e1501489 (2016).
31. J. Kiessling, I. Breunig, P. G. Schunemann, K. Buse, and K. L. Vodopyanov, "High power and spectral purity continuous-wave photonic THz source tunable from 1 to 4.5 THz for nonlinear molecular spectroscopy," New J. Phys. **15**, 105014 (2013).
32. Y.-S. Jang, H. Liu, J. Yang, M. Yu, D.-L. Kwong, and C. W. Wong, "Nanometric precision distance metrology via hybrid spectrally resolved and homodyne interferometry in a single soliton frequency microcomb," Phys. Rev. Lett. **126**, 023903 (2021).
33. J. Riemensberger, A. Lukashchuk, M. Karpov, W. Weng, E. Lucas, J. Liu, and T. J. Kippenberg, "Massively parallel coherent laser ranging using a soliton microcomb," Nature **581**, 164–170 (2020).
34. P. Marin-Palomo, J. N. Kemal, M. Karpov, A. Kordts, J. Pfeifle, M. H. P. Pfeiffer, P. Trocha, S. Wolf, V. Brasch, M. H. Anderson, R. Rosenberger, K. Vijayan, W. Freude, T. J. Kippenberg, and C. Koos, "Microresonator-based solitons for massively parallel coherent optical communications," Nature **546**, 274–279 (2017).
35. A. Fülöp, M. Mazur, A. Lorences-Riesgo, Ó. B. Helgason, P.-H. Wang, Y. Xuan, D. E. Leaird, M. Qi, P. A. Andrekson, A. M. Weiner, and V. Torres-Company, "High-order coherent communications using mode-locked dark-pulse Kerr combs from microresonators," Nat. Commun. **9**, 1598 (2018).
36. B. Corcoran, M. Tan, X. Xu, A. Boes, J. Wu, T. G. Nguyen, S. T. Chu, B. E. Little, R. Morandotti, A. Mitchell, and D. J. Moss, "Ultra-dense

optical data transmission over standard fibre with a single chip source," Nat. Commun. **11**, 2568 (2020).
37. T. J. Kippenberg, A. L. Gaeta, M. Lipson, and M. L. Gorodetsky, "Dissipative Kerr solitons in optical microresonators," Science **361**, eaan8083 (2018).
38. S. Miller, K. Luke, Y. Okawachi, J. Cardenas, A. L. Gaeta, and M. Lipson, "On-chip frequency comb generation at visible wavelengths via simultaneous second- and third-order optical nonlinearities," Opt. Express **22**, 26517–26525 (2014).
39. A. E. Dorche, S. Abdollahramezani, H. Taheri, A. A. Eftekhar, and A. Adibi, "Extending chip-based Kerr-comb to visible spectrum by dispersive wave engineering," Opt. Express **25**, 22362–22374 (2017).
40. Y. Xuan, Y. Liu, L. T. Varghese, A. J. Metcalf, X. Xue, P.-H. Wang, K. Han, J. A. Jaramillo-Villegas, A. Al Noman, C. Wang, S. Kim, M. Teng, Y. J. Lee, B. Niu, L. Fan, J. Wang, D. E. Leaird, A. M. Weiner, and M. Qi, "High-*Q* silicon nitride microresonators exhibiting low-power frequency comb initiation," Optica **3**, 1171–1180 (2016).
41. H. Zhou, S.-W. Huang, Y. Dong, M. Liao, K. Qiu, and C. W. Wong, "Stability and intrinsic fluctuations of dissipative cavity solitons in Kerr frequency microcombs," IEEE Photon. J. **7**, 3200113 (2015).
42. S.-W. Huang, H. Liu, J. Yang, M. Yu, D.-L. Kwong, and C. W. Wong, "Smooth and flat phase-locked Kerr frequency comb generation by higher order mode suppression," Sci. Rep. **6**, 26255 (2016).
43. A. Kordts, M. H. P. Pfeiffer, H. Guo, V. Brasch, and T. J. Kippenberg, "Higher order mode suppression in high-*Q* anomalous dispersion SiN microresonators for temporal dissipative Kerr soliton formation," Opt. Lett. **41**, 452–455 (2016).
44. H. Guo, M. Karpov, E. Lucas, A. Kordts, M. H. P. Pfeiffer, V. Brasch, G. Lihachev, V. E. Lobanov, M. L. Gorodetsky, and T. J. Kippenberg, "Universal dynamics and deterministic switching of dissipative Kerr solitons in optical microresonators," Nat. Phys. **13**, 94–102 (2017).
45. H. Zhou, Y. Geng, W. Cui, S. W. Huang, Q. Zhou, K. Qiu, and C. W. Wong, "Soliton bursts and deterministic dissipative Kerr soliton generation in auxiliary-assisted microcavities," Light Sci. Appl. **8**, 50 (2019).
46. E. Lucas, H. Guo, J. D. Jost, M. Karpov, and T. J. Kippenberg, "Detuning-dependent properties and dispersion-induced instabilities of temporal dissipative Kerr solitons in optical microresonators," Phys. Rev. A **95**, 043822 (2017).
47. J. Liu, A. S. Raja, M. Karpov, B. Ghadiani, M. H. P. Pfeiffer, B. Du, N. J. Engelsen, H. Guo, M. Zervas, and T. J. Kippenberg, "Ultralow-power chip-based soliton microcombs for photonic integration," Optica **5**, 1347–1353 (2018).
48. G. Lihachev, J. Liu, W. Weng, L. Chang, J. Guo, J. He, R. N. Wang, M. H. Anderson, J. E. Bowers, and T. J. Kippenberg, "Platicon microcomb generation using laser self-injection locking," Nat. Commun. **13**, 1771 (2022).
49. J. Liu, G. Huang, R. N. Wang, J. He, A. S. Raja, T. Liu, N. J. Engelsen, and T. J. Kippenberg, "High-yield, wafer-scale fabrication of ultralow-loss, dispersion-engineered silicon nitride photonic circuits," Nat. Commun. **12**, 2236 (2021).
50. W. Jin, Q.-F. Yang, L. Chang, B. Shen, H. Wang, M. A. Leal, L. Wu, M. Gao, A. Feshali, M. Paniccia, K. J. Vahala, and J. E. Bowers, "Hertz-linewidth semiconductor lasers using CMOS-ready ultra-high-*Q* microresonators," Nat. Photonics **15**, 346–353 (2021).
51. S.-W. Huang, H. Zhou, J. Yang, J. F. McMillan, A. Matsko, M. Yu, D.-L. Kwong, L. Maleki, and C. W. Wong, "Mode-locked ultrashort pulse generation from on-chip normal dispersion microresonators," Phys. Rev. Lett. **114**, 053901 (2015).
52. A. B. Matsko, A. A. Savchenkov, and L. Maleki, "Normal group-velocity dispersion Kerr frequency comb," Opt. Lett. **37**, 43–45 (2012).
53. C. Godey, I. V. Balakireva, A. Coillet, and Y. K. Chembo, "Stability analysis of the spatiotemporal Lugiato-Lefever model for Kerr optical frequency combs in the anomalous and normal dispersion regimes," Phys. Rev. A **89**, 063814 (2014).
54. W. Liang, A. A. Savchenkov, V. S. Ilchenko, D. Eliyahu, D. Seidel, A. B. Matsko, and L. Maleki, "Generation of a coherent near-infrared Kerr frequency comb in a monolithic microresonator with normal GVD," Opt. Lett. **39**, 2920–2923 (2014).
55. A. Rizzo, A. Novick, V. Gopal, B. Y. Kim, X. Ji, S. Daudlin, Y. Okawachi, Q. Cheng, M. Lipson, A. L. Gaeta, and K. Bergman, "Integrated Kerr frequency comb-driven silicon photonic transmitter," arXiv:2109.10297 (2021).
56. H. Shu, L. Chang, Y. Tao, B. Shen, W. Xie, M. Jin, A. Netherton, Z. Tao, X. Zhang, R. Chen, B. Bai, J. Qin, S. Yu, X. Wang, and J. E. Bowers, "Bridging microcombs and silicon photonic engines for optoelectronics systems," Nature **605**, 457–463 (2022).
57. V. E. Lobanov, G. Lihachev, T. J. Kippenberg, and M. L. Gorodetsky, "Frequency combs and platicons in optical microresonators with normal GVD," Opt. Express **23**, 7713–7721 (2015).
58. Y. Liu, Y. Xuan, X. Xue, P.-H. Wang, S. Chen, A. J. Metcalf, J. Wang, D. E. Leaird, M. Qi, and A. M. Weiner, "Investigation of mode coupling in normal-dispersion silicon nitride microresonators for Kerr frequency comb generation," Optica **1**, 137–144 (2014).
59. X. Xue, Y. Xuan, P.-H. Wang, Y. Liu, D. E. Leaird, M. Qi, and A. M. Weiner, "Normal-dispersion microcombs enabled by controllable mode interactions," Laser Photon. Rev. **9**, L23–L28 (2015).
60. Ó. B. Helgason, F. R. Arteaga-Sierra, Z. Ye, K. Twayana, P. A. Andrekson, M. Karlsson, J. Schröder, and V. Torres-Company, "Dissipative solitons in photonic molecules," Nat. Photonics **15**, 305–310 (2021).
61. V. E. Lobanov, A. V. Cherenkov, A. E. Shitikov, I. A. Bilenko, and M. L. Gorodetsky, "Dynamics of platicons due to third-order dispersion," Eur. Phys. J. D **71**, 185 (2017).
62. V. E. Lobanov, A. E. Shitikov, R. R. Galiev, K. N. Min'kov, and N. M. Kondratiev, "Generation and properties of dissipative Kerr solitons and platicons in optical microresonators with backscattering," Opt. Express **28**, 36544–36558 (2020).
63. A. M. Kaplan, G. P. Agrawal, and D. N. Maywar, "Optical square-wave clock generation based on an all-optical flip-flop," IEEE Photon. Technol. Lett. **22**, 489–491 (2010).
64. L. K. Oxenlowe, R. Slavik, M. Galili, H. C. H. Mulvad, A. T. Clausen, Y. Park, J. Azana, and P. Jeppesen, "640 Gb/s timing jitter-tolerant data processing using a long-period fiber-grating-based flat-top pulse shaper," IEEE J. Sel. Top. Quantum Electron. **14**, 566–572 (2008).
65. E. Palushani, L. K. Oxenlowe, M. Galili, H. Mulvad, A. T. Clausen, and P. Jeppesen, "Flat-top pulse generation by the optical Fourier transform technique for ultrahigh speed signal processing," IEEE J. Quantum Electron. **45**, 1317–1324 (2009).
66. V. V. Lozovoy, G. Rasskazov, A. Ryabtsev, and M. Dantus, "Phase-only synthesis of ultrafast stretched square pulses," Opt. Express **23**, 27105–27112 (2015).
67. M. H. Anderson, G. Lihachev, W. Weng, J. Liu, and T. J. Kippenberg, "Zero-dispersion Kerr solitons in optical microresonators," arXiv:2007.14507 (2020).
68. V. E. Lobanov, G. Lihachev, and M. L. Gorodetsky, "Generation of platicons and frequency combs in optical microresonators with normal GVD by modulated pump," Europhys. Lett. **112**, 54008 (2015).
69. H. Liu, S.-W. Huang, J. Yang, M. Yu, D.-L. Kwong, and C. W. Wong, "Bright square pulse generation by pump modulation in a normal GVD microresonator," in *Conference on Lasers and Electro-Optics* (OSA, 2017), paper FTu3D.3.
70. A. Antikainen and G. P. Agrawal, "Dual-pump frequency comb generation in normally dispersive optical fibers," J. Opt. Soc. Am. B **32**, 1705–1711 (2015).
71. C. Finot, B. Kibler, L. Provost, and S. Wabnitz, "Beneficial impact of wave-breaking for coherent continuum formation in normally dispersive nonlinear fibers," J. Opt. Soc. Am. B **25**, 1938–1948 (2008).
72. J. Fatome, C. Finot, G. Millot, A. Armaroli, and S. Trillo, "Observation of optical undular bores in multiple four-wave mixing," Phys. Rev. X **4**, 021022 (2014).
73. W. Weng, E. Lucas, G. Lihachev, V. E. Lobanov, H. Guo, M. L. Gorodetsky, and T. J. Kippenberg, "Spectral purification of microwave signals with disciplined dissipative Kerr solitons," Phys. Rev. Lett. **122**, 013902 (2019).